AIAA

AD-A268 648

AIAA 93-3526
Characteristics of Deformable Leading Edge for High Performance Rotor

S. Lee, K. W. McAlister, and C. Tung
U. S. Army Aeroflightdynamics Directorate
ATCOM, NASA-Ames Research Center
Moffett Field, California 94035

DTIC
ELECTE
AUG 3 0 1993
S D
A

93-19878

93 8 24 207

AIAA 11th Applied Aerodynamics Conference
August 9-11, 1993 / Monterey, CA

CHARACTERISTICS OF DEFORMABLE LEADING EDGE
FOR HIGH PERFORMANCE HELICOPTER ROTOR

Soogab Lee[*], K. W. McAlister[†], Chee Tung [†]
U.S. Army Aeroflightdynamics Directorate, ATCOM
NASA Ames Research Center, Moffett Field, California, 94035

Abstract

The deformable leading edge (DLE) concept to improve the blade capability in lift, drag and pitching moments has been investigated for the purpose of meeting new rotor maneuverability and susceptibility requirements. The advantages and disadvantages of this concept have been carefully examined with limited computational and experimental results. This work showed that this concept achieves a substantial improvement in lift capability and also reduces the drag and pitching moment at the same time. Effects of various parameters, such as Reynolds number, reduced frequency, mean angle of oscillation, and airfoil shape, on the performance of these airfoils were also investigated.

Introduction

In forward flight, helicopter rotor blades experience an angle of attack change from a relatively small value on the advancing sides to a relatively large value on the retreating side. Under certain flight conditions, the rotor encounters dynamic stall. Dynamic stall limits the performance of helicopters by causing severe vibratory loads due to abrupt changes in lift, drag and pitching moment. This load condition has been avoided in the past by defining a flight envelope which keeps the aircraft from operating in the region of dynamic stall.

However, helicopters are now being considered for tasks which require vehicle designers to consider a dramatic increase in the performance envelope. Thus, innovative ideas must be incorporated in the blade design to delay or suppress dynamic stall. (See Ref.1 for more details)

In order to meet these requirements, computational and experimental works[2] have been initiated at AFDD to evaluate the effectiveness of various concepts such as airfoil slots/slats[3,4], deformable leading-edge, upper surface blowing (constant and cyclic), flaperon, and blade flaps. In this paper, only the deformable leading-edge concept will be discussed. The objective of DLE (Fig. 1) is to delay or suppress dynamic stall by drooping the leading-edge at a high angle-of-attack and making the flow pass smoothly around the leading-edge. To investigate the static and dynamic characteristics of DLE, an incompressible Navier-Stokes code (named ZETA), based on a velocity-vorticity formulation, was modified to treat a deforming airfoil. For the experimental part, the Army water tunnel at Ames was utilised to measure the quasi-steady and unsteady loads on the airfoil during the pitch oscillations. The influence of Reynolds number, airfoil shape, mean angle of oscillation, droop angle and center of rotation, and reduced frequency on the DLE performance was also investigated.

Description of the Experiment

This study was conducted in the 4000-liter, closed-circuit water tunnel facility at the Aeroflightdynamics Directorate, Ames Research Center (Fig. 2). This was a particularly suitable facility for this investigation because of the ease of obtaining definitive visualisations of the flow and the advantage of examining on-line the resultant loads on the airfoil. The technique for visualising the flow was based on the release of a fluorescing dye through an orifice located at the leading edge of the airfoil. Loads were measured directly by an exter-

---

1

nal apparatus that served as both support and balance for the airfoil.

Two airfoils were selected for this study. The first was a VR-12 having a two-dimensional planform of 10 cm (chord) by 21 cm (span). The second was a modified VR-12 with a droop angle of 13° (case 2513). Both airfoils are shown in Fig. 3. The test section measures 31 cm (height) by 21 cm (width), and the airfoil was positioned so that it spanned the width of the section to within 0.015 cm on either side. The main body of the airfoil was cast from urethane and the spar was made from stainless steel.

The spar of the airfoil extended through the test-section windows and was supported by lift and drag transducers on both sides (Fig. 4). One end of the spar was adjoined to an instrumented drive shaft through a torsionally stiff coupling so that airfoil incidence could be set and the pitching moment measured. Static frictional moments imparted by the support bearings and seals were also measured and treated as load tares. Only quantities relating to the airfoil were electrically instrumented, and these were incidence, lift (both sides), drag (both sides), total pitching moment, and the bearing and seal moments (both sides). After amplification, the signals were were transmitted to a data acquisition system where they were digitised, averaged, and stored for later processing. It is estimated that airfoil incidence was measured to an accuracy of 0.2° during the test. Lift and drag measurements are considered to be accurate to 0.01 newtons and the pitching moments accurate to 0.002 newton-m.

The dye was illuminated by an xenon strobe during single-frame exposures and by an argon-ion laser during video exposures. In both cases, the light sheet was about 2 cm wide and was directed through the upper test-section window and across the flow above the airfoil. The dye that was released from the leading edge of the airfoil was transported downstream by the fluid in the boundary layer and wake, thereby enabling the thickness and eventual separation of the boundary layer to be observed.

The tunnel was operated at an average dynamic pressure of 0.019 kg/cm^2, which for an ambient temperature of 21°C and an airfoil chord of 10 cm gives a Reynolds number of 200,000. The unsteady measurements of lift, drag, pitching moment were made with $\alpha = 15° + 10° \sin(2\pi ft)$ and at a reduced frequency k. The reduced frequency, k, is related to the oscillating frequency, f, by the expression $k = \pi fc/v_\infty$, where c is the chord length and v_∞ is the free stream velocity.

Description of the Theory

The ZETA[5] code uses the vorticity vector as the primary variable. By doing so, the computation of an unsteady flow field can be partitioned into its kinematic and kinetic parts. In the kinematic part, the velocity field is related to the vorticity field at any instant of time by the continuity equation and the curl of the velocity. They are

$$\nabla \cdot \vec{v} = 0 \qquad (1)$$

$$\nabla \times \vec{v} = \vec{\omega} \qquad (2)$$

In the kinetic part, the vorticity is computed at each time step by solving the vorticity transport equation, which is

$$\frac{\partial \vec{\omega}}{\partial \tau} = -(\vec{v} \cdot \nabla)\vec{\omega} + \nabla \cdot (\nu \nabla \vec{\omega}) \qquad (3)$$

where $\vec{v}$ and $\vec{\omega}$ are the velocity and vorticity vectors respectively; τ denotes the time and ν represents the kinematic viscosity of the fluid. When the flow is turbulent ν includes the eddy viscosity, and in this case the Baldwin-Lomax model (Ref. 6) is used. Eqs. (1) and (2) can be recast into an integral form for the velocity vector using the fundamental solution of an elliptic equation:

$$\vec{v}(\vec{r}, \tau) = - \int_R \vec{\omega}_o \times \vec{Q} dR_o$$
$$+ \int_S [(\vec{v}_o \cdot \vec{n}_o) - (\vec{v}_o \times \vec{n}_o) \times] \vec{Q} dB_o + \vec{v}_\infty \qquad (4)$$

where $\vec{r}$ is a position vector and $\vec{v}_\infty$ is the free stream velocity; R is the fluid domain contained between the far stream boundary and the solid surface S; $\vec{n}$ is a unit normal vector on S directed outward into R; the subscript "o" indicates that a variable or an integration is in the $\vec{r}_o$ space; and $\vec{Q}$ is the gradient of the fundamental solution. For two dimensional flows,

$$\vec{Q} = \frac{\vec{r}_o - \vec{r}}{2\pi |\vec{r}_o - \vec{r}|^2} \qquad (5)$$

It should be noticed from Eqs. (3) and (4) that the computation of any unsteady flow problem can be confined to the vortical region (without regard for the remainder of the flow field). This ability offers a significant savings in both computer time and storage. For the present study of dynamic stall, the vortical flow region consists of the attached, the separated and wake zones. Whenever the flow is attached, a boundary layer solver is employed to increase the computing efficiency. The

vorticity values on the solid surface require special consideration since the non-slip boundary condition on the solid surface is required for the velocity field. As shown in Ref. 7, the boundary vorticity values are obtained evaluating Eq. (4) on S,

$$\vec{v}(\vec{r}_S, \tau) = -\int_{S+} \vec{\gamma}_o \times \vec{Q} dR_o$$
$$-\int_{R-} \vec{\omega}_o \times \vec{Q} dR_o \qquad (6)$$
$$+\int_S [(\vec{v}_o \cdot \vec{n}_o) - (\vec{v}_o \times \vec{n}_o) \times]\vec{Q} dB_o + \vec{v}_\infty$$

where $\vec{r}_S$ is a position vector on the solid surface S where the vorticity is unknown. The domain integral over R in Eq. (4) is divided into two parts: one is the integral over an infinitesimal thin layer S^+ adjacent to S containing the unknown vorticity, and the other is the integral over the remaining vortical region R^-. The unknown vorticity within the infinitesimally thin layer is represented by the vortex sheet strength γ. The strength γ can be determined from Eq. (6) if the vorticity distribution in R^- and velocity on S are known. The conservation of the total vorticity is needed to determine the strength uniquely.

The numerical procedure incorporates a conformal mapping to transfer the physical domain onto a simple region with suitable computation grids. The initial solution starts from a potential flow solution around the solids undergoing an impulsive start motion. A time marching procedure computes the initial vortex sheet strength γ in the infinitesimally thin layer surrounding the solids. The velocity field corresponding to this initial vorticity field is computed by Eq. (4). The vorticity is then diffused from the thin layer and convected away by the velocity field. The process is repeated at each time step until either a converged or a periodic solution is reached. A detailed description of the mathematical formulation, conformal transformation and solution procedure is given in Ref. 5. The procedure to solve the variable-droop leading-edge airfoil requires the conformal transformation of the airfoil coordinates at each time step.

Results and Discussion

Effects of droop angle and center of rotation

The deformable leading-edge (DLE) approach to delaying or suppressing the dynamic stall is based on

drooping the leading-edge part of the airfoil at high angles of attack so that the flow passes smoothly around the leading-edge. There are two geometric parameters describing the drooped leading-edge; one is the center of rotation(z_c) and the other is the droop angle(θ), as illustrated in Fig. 1. In our notation, for example, case 2513 means that the center of rotation is located at 25 % of the chord and the droop angle is 13°. A series of numerical tests of the static and dynamic performances of drooped VR-12 airfoils was carried out, with the center of rotation and the droop angle as parameters, at a Reynolds number of 200,000 and a reduced frequency of 0.1. Dynamic lift, drag, and pitching moments during an oscillation, with the droop angle and the center of rotation as parameters, are shown in Fig. 5 and Fig. 6. The results indicate the following:

(1) As the droop angle increases with a fixed center of rotation, the stall angle and the maximum lift decreases, but the drag and pitching moments are also greatly reduced. When the droop angle increases beyond 15°, the drag and pitching moment are not no longer reduced and the stall angle continues to decrease. (See Fig.5)

(2) As the center of rotation moves rearward ($z_c = .15 \rightarrow .25$) with a fixed droop angle ($\theta = 15°$), the stall angle increases and maximum drag and pitching moments are reduced. (See Fig. 6)

(3) Based on a variation of the droop angle and the center of rotation, case 2513 appears to be superior to the no droop case, offering a reduction in drag and pitching moment and an increase in lift. (See Fig. 7) Note that case 2513 also turned out to be the best case for Re=2,000,000 following a similar parametric study. (see Lee and McAlister[8] for details)

Water tunnel measurements of the basic VR-12 and a drooped VR-12 (case 2513) airfoil are compared with the computed results in Fig. 7. In the experiment, case 2513 showed a significant decrease in lift hysteresis with about 40 % of reduction in the magnitude of the drag and pitching moment. The gain in overall lift (integrated over the cycle of oscillation) was achieved mainly on the downstroke since the stall is delayed and attenuated by drooping the leading edge. On the other hand, the computed results predicted earlier stalls in both cases (especially in a drooped case), and consequently overestimated the drag and pitching moments reductions.

Verification of computational results

In this section, the experimental results from the water tunnel test are compared with the predicted re-

sults. Fig. 8 shows a comparison of experimental and computational flow visualisations of the basic VR-12 airfoil at conditions of $Re = 200,000., \alpha = 15° + 10° \sin \omega t$, and $k = 0.1$. Up to 15° on the upstroke the flow remains attached in both cases. Starting at an angle of 20°, the experiment shows a much larger separated region than does the computation.

The pitching moment hysteresis, rather than the lift hysteresis, might be a more reasonable measure of the prediction capability of a code[9]. Following this point of view, the code seems not to predict the stall onset accurately, but the overall accuracy is acceptable (Fig. 7). One place that is easy to blame for the discrepancy is turbulence modeling. Needless to say, turbulence modeling should be improved to simulate the dynamic stall phenomenon accurately. Unfortunately none of the eddy-viscosity turbulence models (from algebraic to two-equation) can predict separation accurately in all cases[10]. Another possible reason is transition modeling. This is particularly true if the Reynolds number is below 500,000 and a separation is followed by a reattachment of the flow, forming what is known as a "separation bubble". This phenomenon can not be properly simulated without an accurate transition model. As an example, Fig.9 shows a comparison between experimental and computational results for a very slow oscillation (quasi-steady). Measurement of the stall onset reveals a significant discrepancy from the calculated results wherein the flow was set to be fully turbulent. In many cases, experimentalists will trip the airfoil to induce artificial transition at a pre-determined position, which makes it easier to compare with computed results when the code does not have a transition model. A series of experiments for the tripped airfoils, as a extension of the present study, is in progress and will be shown in Ref. 8.

Deformable leading edge at a higher Re

Since a fixed-droop airfoil(case 2513) showed a significant enhancement in lift, drag, and pitching moment hysteresis at a low Reynolds number ($Re = 200,000$), it is worth while to investigate the performance at a higher Reynolds number ($Re = 2,000,000$). For this investigation at the present stage, the ZETA code was used to explore two situations. One is a fixed-droop leading-edge airfoil (case 2513) and the other is a variable-droop leading-edge airfoil (VDLE hereafter). The VDLE concept is desirable for keeping the original shape until the airfoil meets an angle of attack slightly below the stall angle in order to obtain as high a lift as possible on the upstroke. In this section, the detailed results

for a fixed-droop (case 2513) and a VDLE airfoil are described. The conditions are $Re = 2,000,000., \alpha = 15° + 10° \sin \omega t$, and $k = 0.1$. For the VDLE case, the droop angle, θ, versus the angle-of-attack, α, was selected as follows:

$$\begin{cases} \theta = \alpha - 13.0 & if & \alpha \geq 13.0 \\ \theta = 0.0 & if & \alpha < 13.0 \end{cases} \quad (7)$$

Before proceeding with the detailed calculation, it should be verified that the code works properly at a Reynolds number of 2,000,000 since the computed results revealed a poor prediction of quasi-steady results at $Re = 200,000$. In Fig. 10, the predicted results for steady angles-of-attack are compared with available experimental data.[11,12] For the NACA 0015 and VR-7 airfoil cases, the computed results predict the stall onset and maximum lift coefficients quite well. Note that both experiments were carried out at a Mach number of 0.1, where compressibility effects should be negligible.

The static lift, drag and pitching moment were calculated and measured at discrete angles from 0° to 30°. The static and dynamic load characteristics of the basic VR-12 airfoil, the drooped VR-12 (case 2513), and a VDLE case are compared in Fig. 11. The static lift coefficient for the no-droop case simply increases until $\alpha = 15°$. Slightly above $\alpha = 16°$, the airfoil stalls, which causes C_l to drop to the minimum value. For case 2513, the airfoil also stalls at $\alpha = 13°$, but the magnitude is much smaller since the stall occurs near the trailing-edge instead of the leading-edge. This airfoil eventually stalls from the leading-edge (at $\alpha = 25°$) and the lift drops quickly. The variable-droop leading-edge (VDLE) case performs much better than the previous two cases in the static mode. A comparison of the drag obtained in these three cases most clearly shows that the drooped airfoil delays the static stall. The drag coefficient for the basic VR-12 shows an abrupt increase at $\alpha = 16°$ due to stall. In case 2513, the drag increases more gradually and reaches a smaller magnitude than obtained in the basic case. For the VDLE case, the drag is generally less than that of case 2513. The pitching moments of both drooped leading-edge airfoils have less variation with angle-of-attack than does the basic case.

To better appreciate the extent of the unsteady hysteresis in the lift curves, the static lift curve (dotted line) for the basic VR-12 airfoil has been included in Fig. 11. For the basic VR12 airfoil, the dynamic stall effect is quite evident. The lift increases almost linearly up to $\alpha = 23°$, then increases rapidly due to the formation of leading-edge stall vortex, and finally experiences a sudden drop due to the shedding of the leading-edge

4

vortex into the downstream wake. Note that the angle of the leading-edge vortex formation is delayed by 2°, as compared with the case at Re= 200,000. When the vortex is detached from the airfoil, the airfoil experiences large fluctuations in lift, drag and pitching moment, as seen in Fig. 11. The lift hysteresis loop for the drooped VR-12 (case 2513) shows that it does not encounter deep dynamic stall, consequently both the drag and the moment hysteresis loops also do not experience any abrupt increase, as compared with the basic VR-12 airfoil. The VDLE case reveals an additional gain in lift on the upstroke and more reduction in drag and pitching moment. Note that the VDLE case generally performs better than case 2513 in the range of low angles-of-attack.

Computed surface pressure distributions and streamlines at selected angles-of- attack during the oscillation for the basic and the drooped VR-12 (case 2513) airfoil are shown in Figs. 12 and 13. The basic VR-12 experiences a strong leading-edge stall at $\alpha = 25°$ and has lost most of the suction peak. On the other hand, the drooped VR-12 (case 2513) experiences only trailing-edge stall even at $\alpha = 25°$, and consequently maintains its suction peak. A comparison of vorticity contours in Fig. 14 indicates that the basic VR-12 induces a large leading-edge separation at $\alpha = 25°$ whereas the drooped airfoil does not.

Effect of reduced frequency

The contrast in performance of the basic and drooped VR-12 (case 2513) airfoil, with the reduced frequency as a parameter, is shown in Fig. 15. The stall angle of the basic airfoil is more sensitive to changes in reduced frequency than that of the drooped airfoil, a trend which is clearly evident in all (lift, drag and pitching moment) hysteresis curves. The magnitudes of the lift and drag coefficients are increased with frequency in both cases. This implies that the performance is enhanced by drooping the leading edge, regardless of the reduced frequency. Note that in the quasi-steady case ($k = 0.0026$), the drooped airfoil does not exhibit any hysteresis in the lift, drag, or pitching moment curves.

Effect of mean angle

Fig. 16 shows the effect of the mean angle of oscillation on the unsteady loads of both the basic and the drooped cases. For the three cases studied ($\alpha_m = 10°, 15°,$ and $20°$), the drooped airfoil has better performance in lift, drag, and pitching moment. However, the improvements obtained for $\alpha_m = 10°$ and $\alpha_m = 20°$

are not as striking as those obtained for $\alpha_m = 15°$. The reason is that the case 2513 was determined as the best configuration for $\alpha_m = 15°$, but not for $\alpha_m = 10°$ or $\alpha_m = 20°$, which implies that the performance enhancement obtained by drooping the leading-edge depends on the mean angle to some extent.

Effect of airfoil shape

To investigate how a different airfoil shape might affect dynamic stall after drooping the leading edge, the SSC-A07 airfoil[13] was selected. In Fig. 17, dynamic lift, drag, and pitching moments are compared for the basic and drooped SSC-A07 airfoils. The overall tendency is very similar to the VR-12 case, which showed that drag and pitching moment are greatly reduced, with some gain in lift, due to a reduction in the magnitude of the dynamic stall.

Conclusions

The present study considered the effect of a deformable leading-edge for dynamic stall control. With limited experimental and computational data, the major concluding remarks are as follows:

(1) By drooping the leading edge during a pitch oscillation, the lift performance can be significantly enhanced and the drag and the pitching moment greatly reduced at both low ($Re = 200,000$) and high ($Re = 2,000,000$) Reynolds numbers. The gain in lift occurs mostly during the downstroke, rather than on the upstroke, as a result of an attenuation of the magnitude of the dynamic stall. The deformable leading-edge also appears to be more effective than the slatted airfoil (see Ref.1) for reducing drag and pitching moment fluctuations.

(2) The benefits from a drooped leading edge are not sensitive qualitatively to the reduced frequency and the airfoil shape, but might be sensitive to the mean angle.

(3) The ZETA code predicted the dynamic stall phenomena quite well qualitatively, but was not exact quantitatively. The code predicted the stall onset reasonably in cases of high Reynolds number, but did not in the cases of low Reynolds number with a low reduced frequency. The discrepancies are partially attributed to the lack of appropriate transition and turbulence models.

(4) As an extension of this study, the compressibility effect on the deformable leading edge should be investigated.

5

References

[1] Carr, L. W. and McCroskey, W. J., "A Review of Recent Advances in Computational and Experimental Analysis of Dynamic Stall," *IUTAM Symposium on Fluid Dynamics of High Angle of Attack*, Tokyo, Japan, Sept. 1992.

[2] Yu, Y. H., Lee, S., McAlister, K. W., Tung, C., and Wang, C. M., "High Lift Concepts for Rotorcraft Applications," *The 49th American Helicopter Society Annual Forum*, St. Louis, MO, May 19-21, 1993.

[3] Tung, C., McAlister, K. W. and Wang, C. M., "Dynamic Stall Study of a Multi-Element Airfoil," Paper 9, *Eighteenth European Rotorcraft Forum*, Avignon, France, Sept. 1992.

[4] Carr, L. W. and McAlister, K. W., "The Effect of a Leading-Edge Slat on the Dynamic Stall of an Oscillating Airfoil", AIAA Paper 83-2533.

[5] Peterson, M. T., Wu, J. C., and Wang, C. M. "ZETA - A Manual for a Computer Code That Uses a Zonal Procedure for Evaluating Turbulent and Laminar Flows", Georgia Institute of Technology Report 87-WU, 1987.

[6] Baldwin, B., and Lomax, H. "Thin Layer Approximation and Algebraic Model for Separated Turbulent Flows", AIAA Paper 78-0257.

[7] Wu, J. C., "Numerical Boundary Conditions for Viscous Flow Problems," *AIAA Journal*, Vol. 14, No. 8, pp. 1042-1049, 1976.

[8] Lee, S. and McAlister, K. W., "Effect of the drooped leading-edge on the stall behavior of a VR-12 airfoil," NASA TP, in preparation.
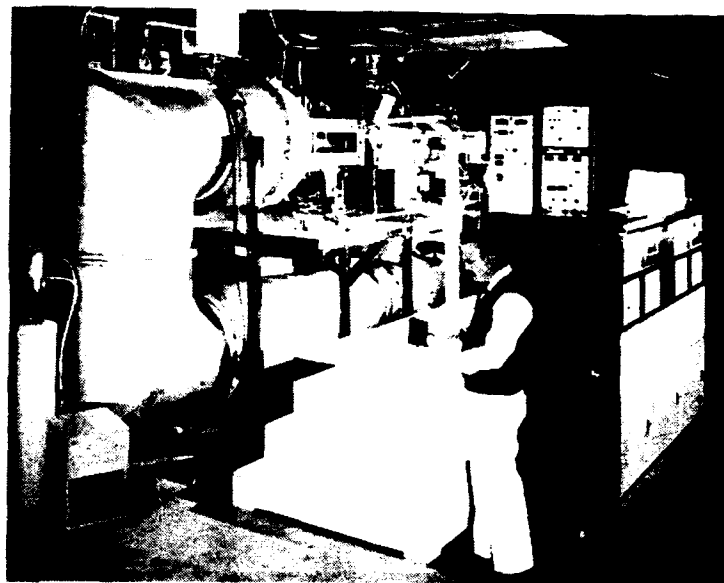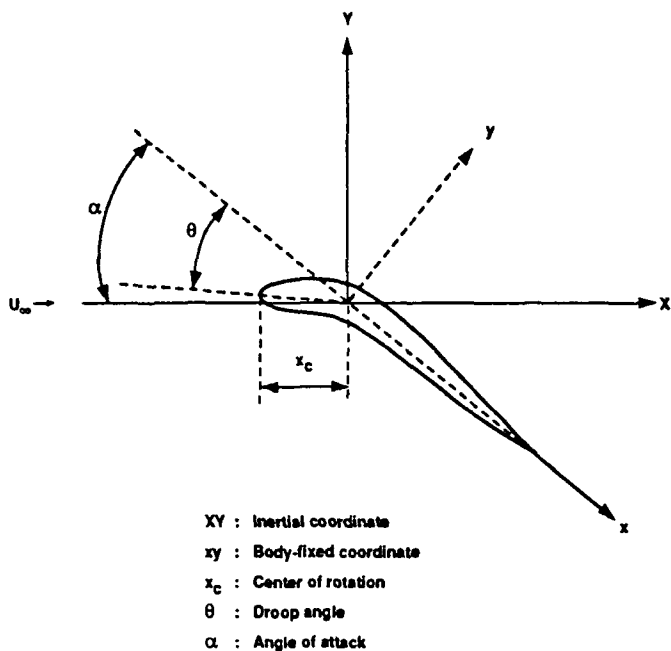
[9] L. W. Carr, Private communications.

[10] Menter, F. R., "Performance of popular Turbulence Models for Attached and Separated Adverse pressure Gradient Flows," AIAA Paper 91-1784, Honolulu, Hawaii, June 1991.

[11] McAlister, K. W., Pucci, S. L., McCroskey, W. J., and Carr, L. W., "An Experimental Study of Dynamic Stall on Advanced Airfoil Sections: Volume 2. Pressure and Force Data," NASA TM 84245, Sep. 1982.

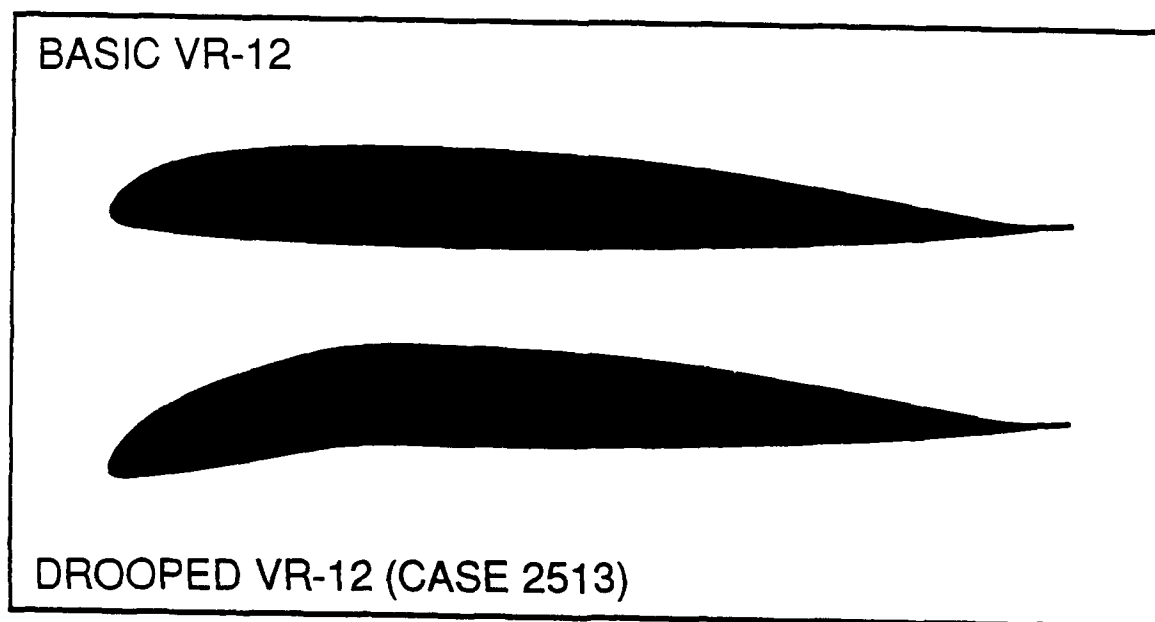[12] Green, R. B. and Galbraith, R., B., "An Investigation of Dynamic Stall through the Application of Leading Edge Roughness," *18th European rotorcraft Forum*, Avignon, France, 1992.

[13] Flemming, R. J., "An Experimental Evaluation of Advanced Rotorcraft Airfoils in The NASA Ames Eleven-Foot Wind Tunnel," NASA CR-166587, Sep. 1984.
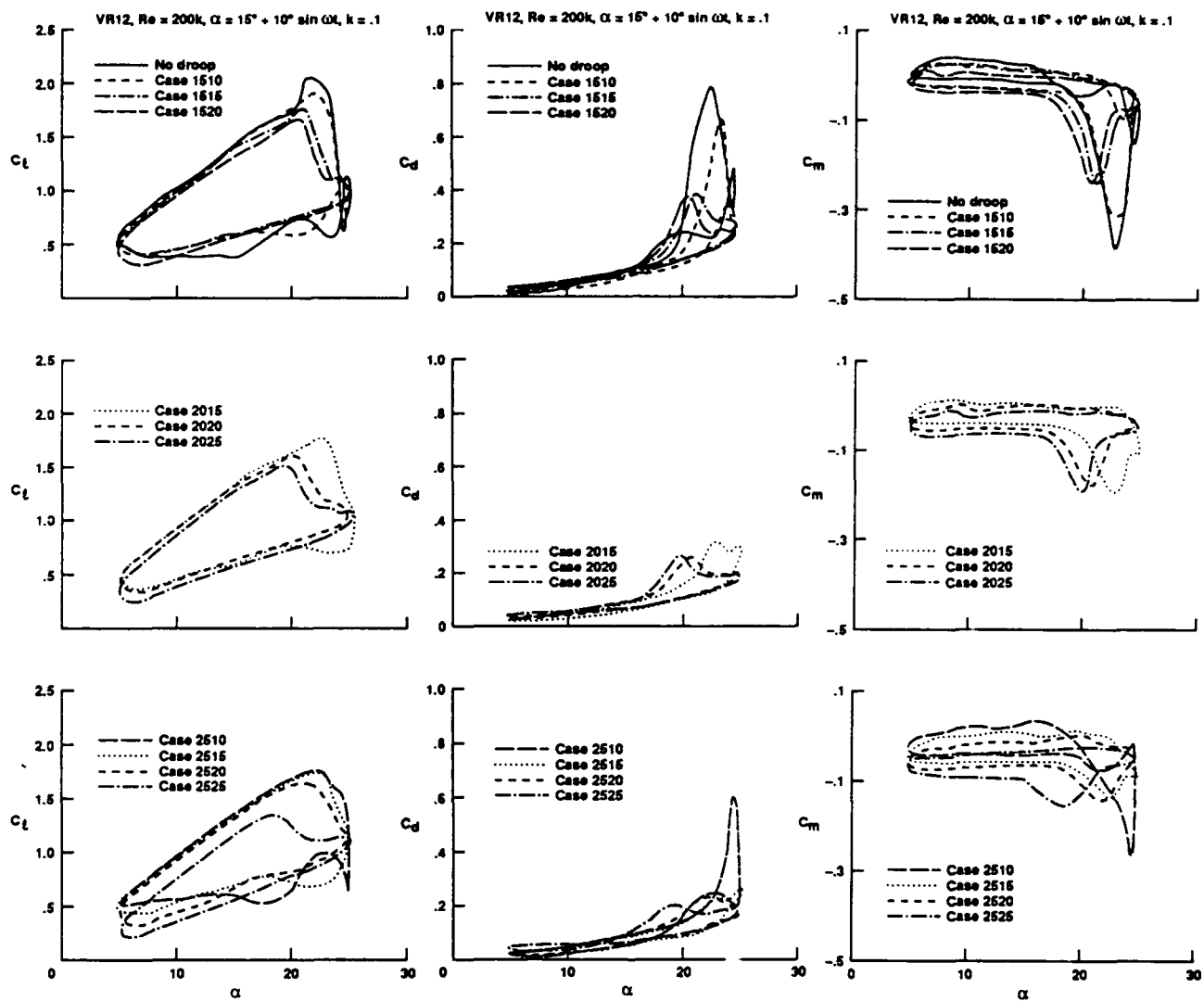
XY : Inertial coordinate
xy : Body-fixed coordinate
x_c : Center of rotation
θ : Droop angle
α : Angle of attack

[Fig. 1] Schematic drawing of drooped leading edge and its coordinates.

[Fig. 2] Water tunnel at NASA-Ames Research Center.

BASIC VR-12

DROOPED VR-12 (CASE 2513)

[Fig. 3] Airfoil shapes of basic and drooped (case 2513) VR-12.

WATER SEAL
MODEL SUPPORT BEARING
WATER INJECTION
TORSION STRAIN-GAGE BRIDGE
STATIONARY
ROTATIONALLY FREE SUPPORT (TYPICAL)
DRAG LOAD CELL
BELLOWS
STATIONARY
STATIONARY
TORSION STRAIN-GAGE BRIDGE
BELLOWS
WATER SEAL
MODEL SUPPORT BEARING
TORSION STRAIN-GAGE BRIDGE
RACK AND GEAR
MODEL SPAR
DRAG LOAD CELL
STATIONARY
LIFT LOAD CELL
FLOW
STATIONARY
ROTATION COUPLING
MODEL INCIDENCE TRANSDUCER
GEAR SUPPORT BEARINGS
LIFT LOAD CELL
STATIONARY
ROTATION COUPLING
MEAN-INCIDENCE ACTUATOR
FLYWHEEL
ECCENTRIC ATTACHMENT FOR OSCILLATION AMPLITUDE

DETAIL OF MODEL SUPPORT

TORSION GAGE
TORSIONALLY STIFF BELLOWS
MODEL
BEARING
MODEL SPAR
LIP SEALS
TEST SECTION WINDOW

[Fig. 4] Drawing of the test section of water tunnel, showing a balance system and model installation.

8

[Fig. 5] Calculated dynamic loads of VR-12, with the droop angle and the center of rotation as parameters, at conditions of $Re = 200,000.$, $\alpha = 15° + 10° sin\omega t$, $k = 0.1$.
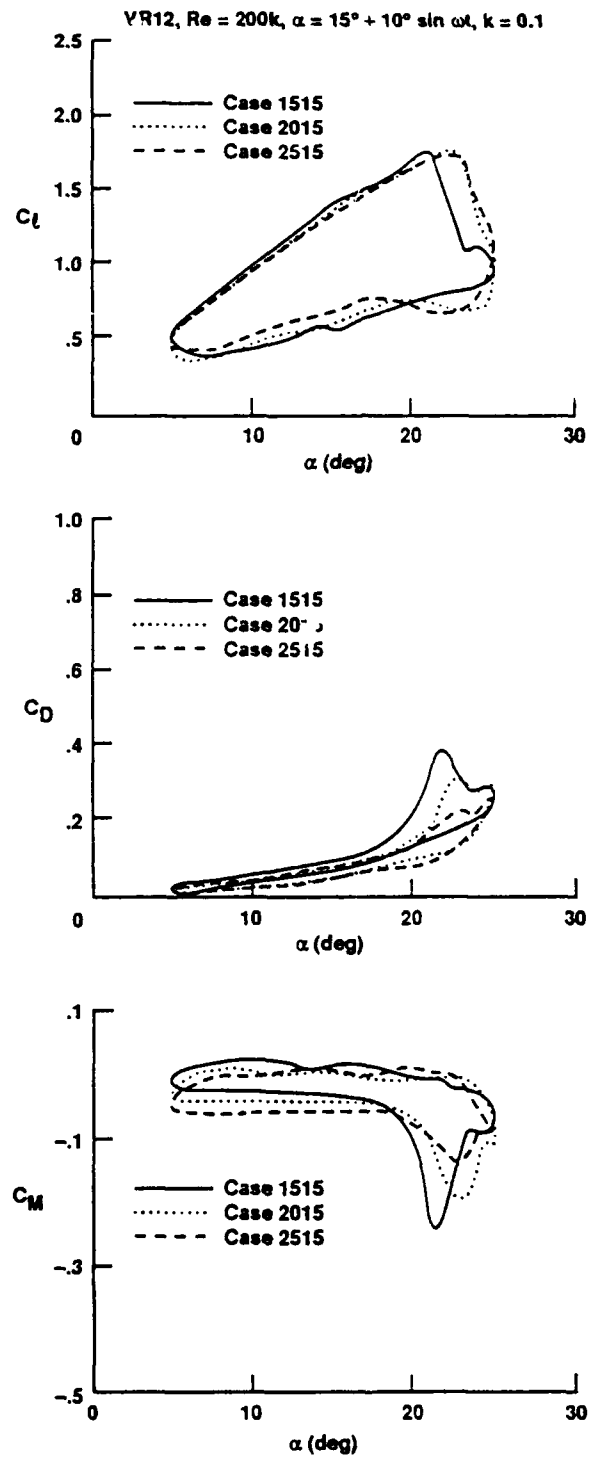
[Fig. 6] Effect of the center of rotation on the calculated dynamic loads, with a fixed droop angle (15°), at conditions of $Re = 200,000., \alpha = 15° + 10° \sin \omega t, k = 0.1$.
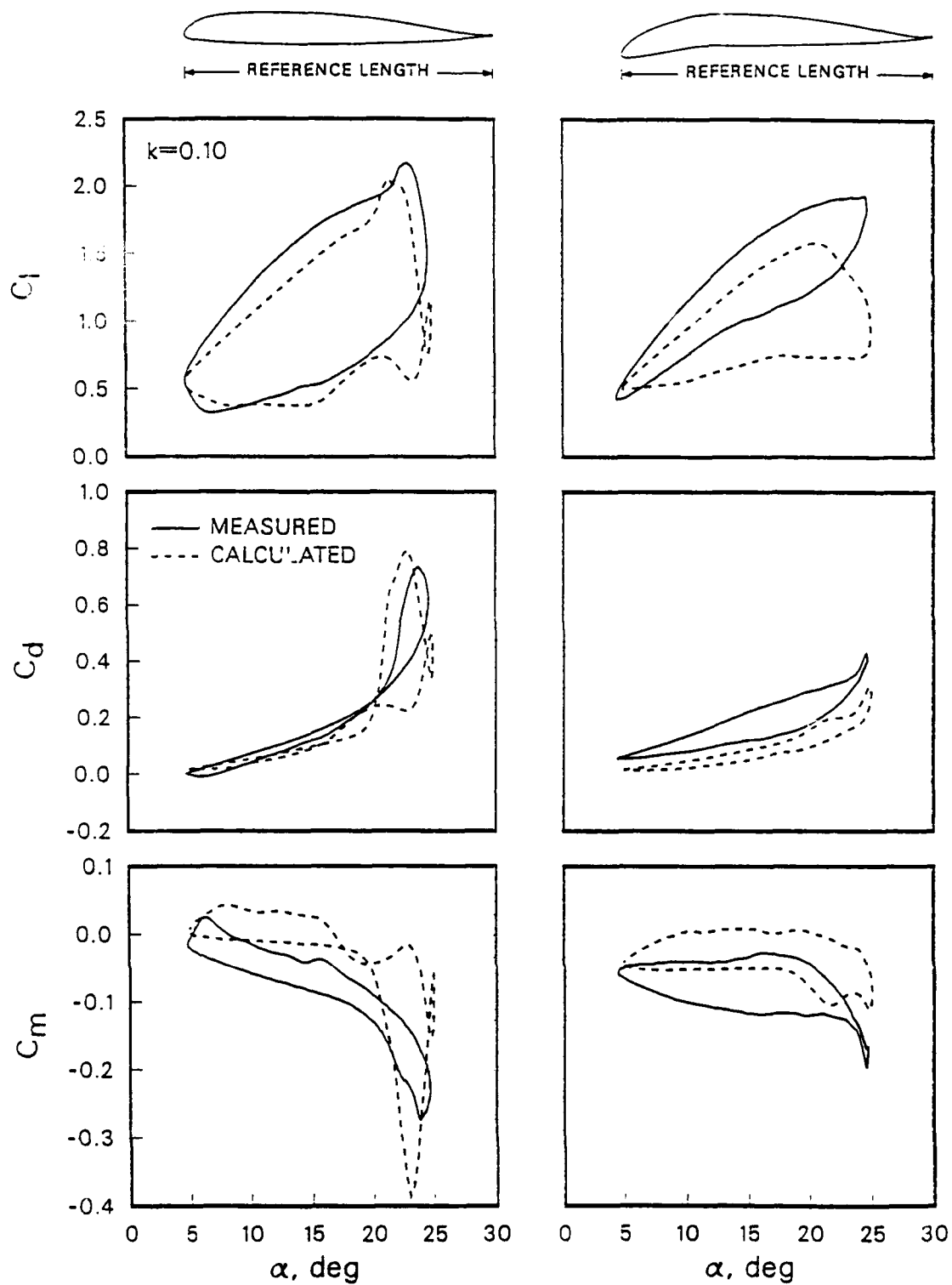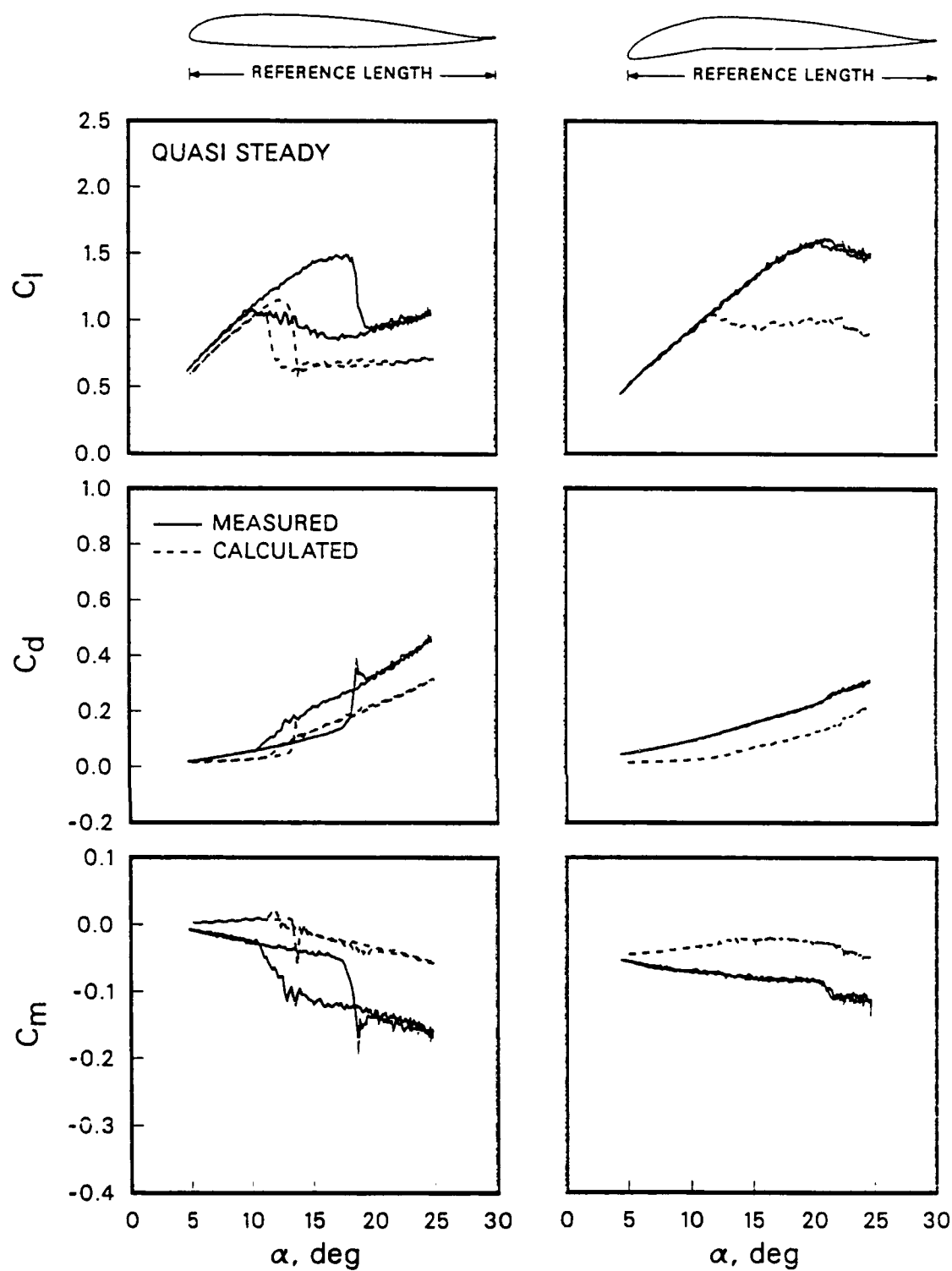
[Fig. 7] Comparison for measured static and dynamic loads of the basic and drooped VR-12 at conditions of $Re = 200,000.$, $\alpha = 15° + 10° sin\omega t$, $k = 0.1$.

Experiment

Computation

α = 5° ↑

$\omega t = -90°$

α = 10° ↑

$\omega t = -45°$

α = 15° ↑

$\omega t = 0°$

α = 20° ↑

$\omega t = 45°$

α = 25°

$\omega t = 90°$

α = 20° ↓

$\omega t = 135°$

α = 15° ↓

$\omega t = 180°$

α = 10° ↓

$\omega t = 225°$
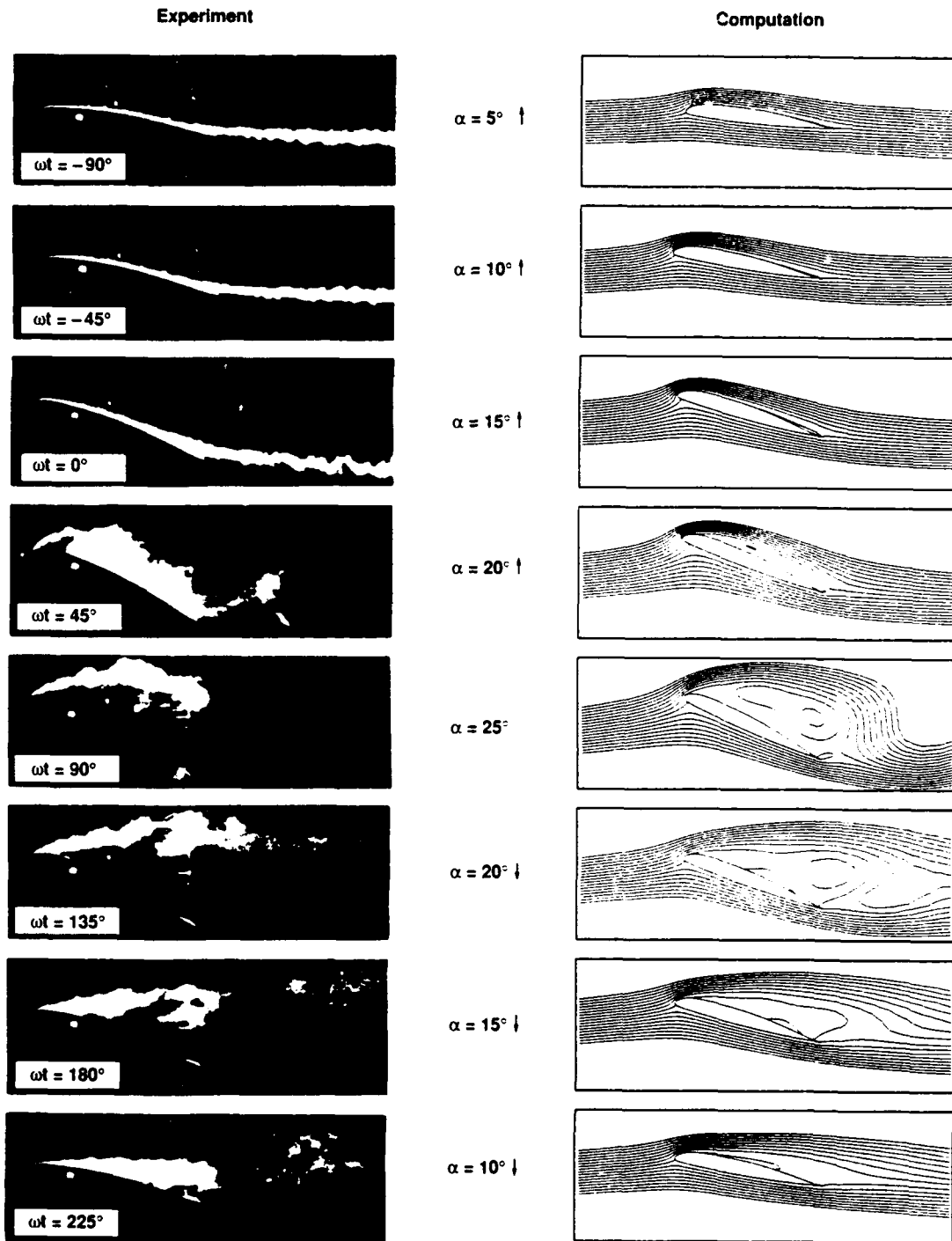
[Fig. 8] Comparison of experimental and computational flow visualisations for the basic and drooped VR-12 airfoils at conditions of $Re = 200,000., \alpha = 15° + 10° sin\omega t, k = 0.1$.

12

[Fig. 9] Comparison of measured and predicted dynamic loads of the basic and drooped (case 2513) VR-12 airfoil in a very slow oscillation ($\alpha = 15° + 15°sin\omega t$ with $k = 0.0026$) at $Re = 200,000$.
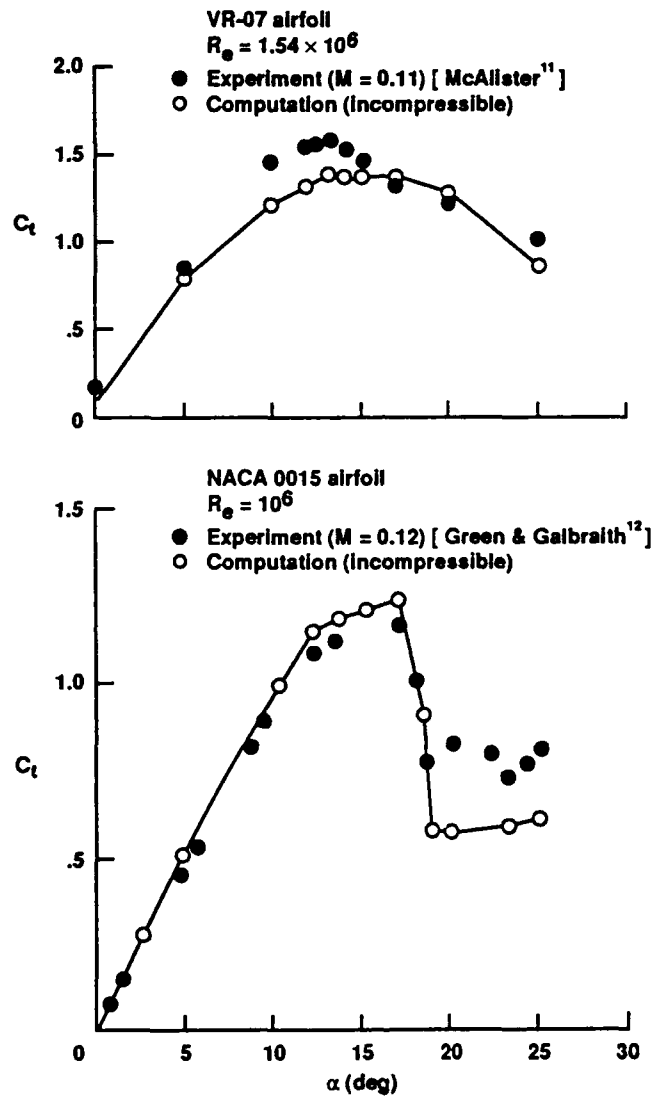
[Fig. 10] Comparison of measured and computed steady lift coefficients of NACA 0015 and VR-7 airfoils at a higher Reynolds number ($Re = 2,000,000$.)
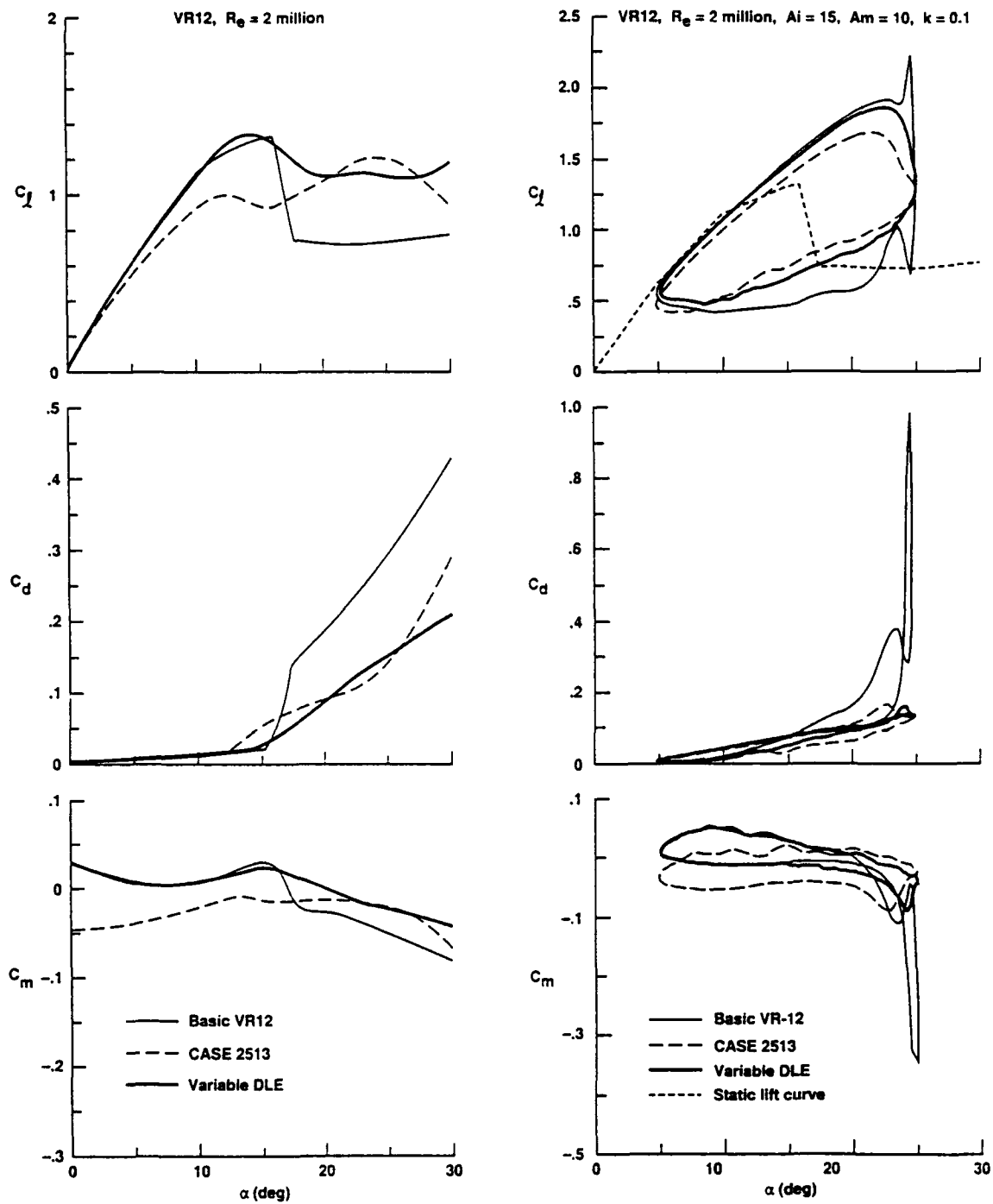
[Fig. 11] Calculated static and dynamic loads of the basic and the drooped (case 2513 and VDLE) VR-12 at conditions of $Re = 2,000,000., \alpha = 15° + 10° sin\omega t, k = 0.1$.

15

Basic VR-12, R_e = 2,000,000., α = 15° + 10° sin ωt, k = 0.1
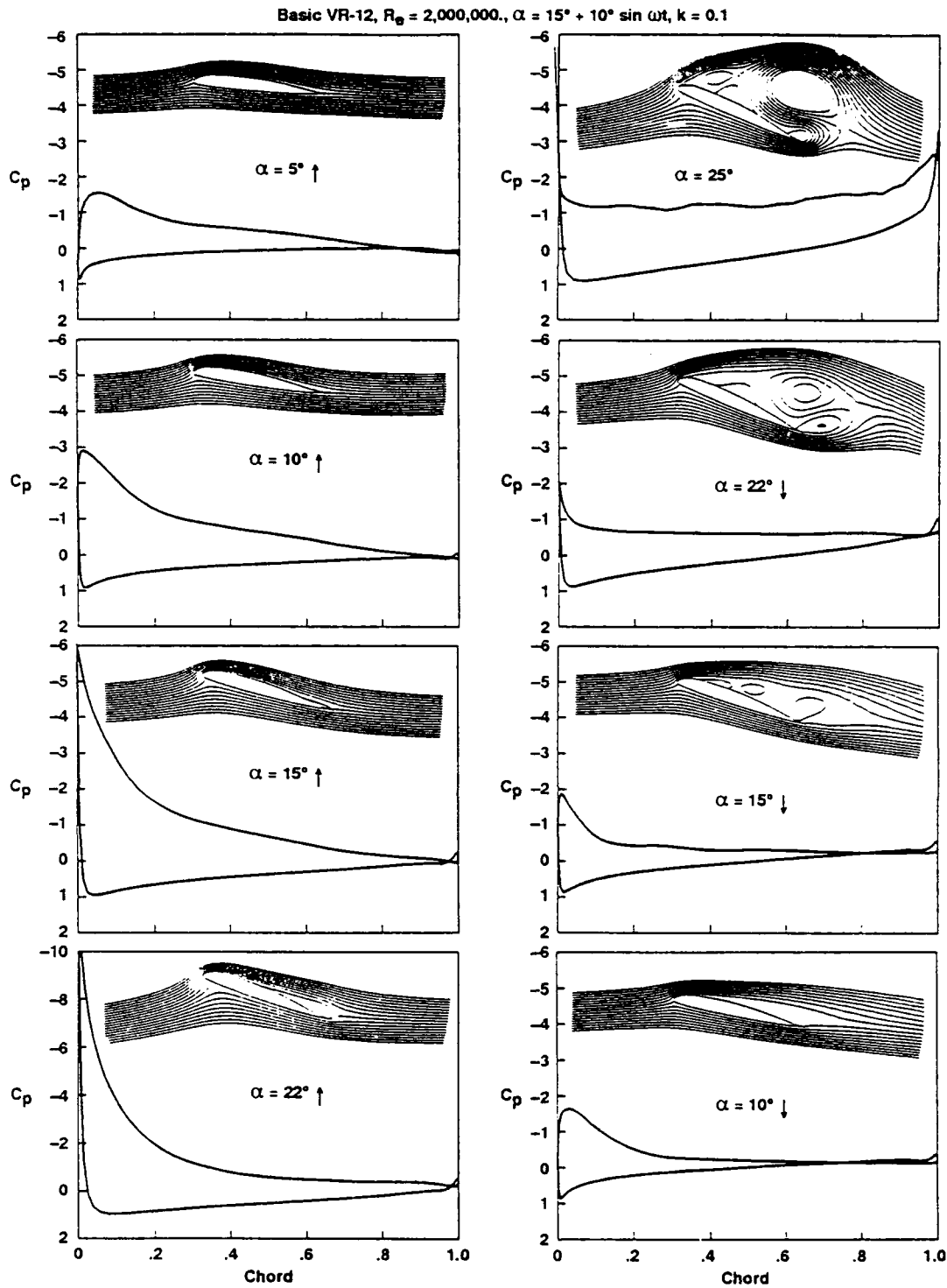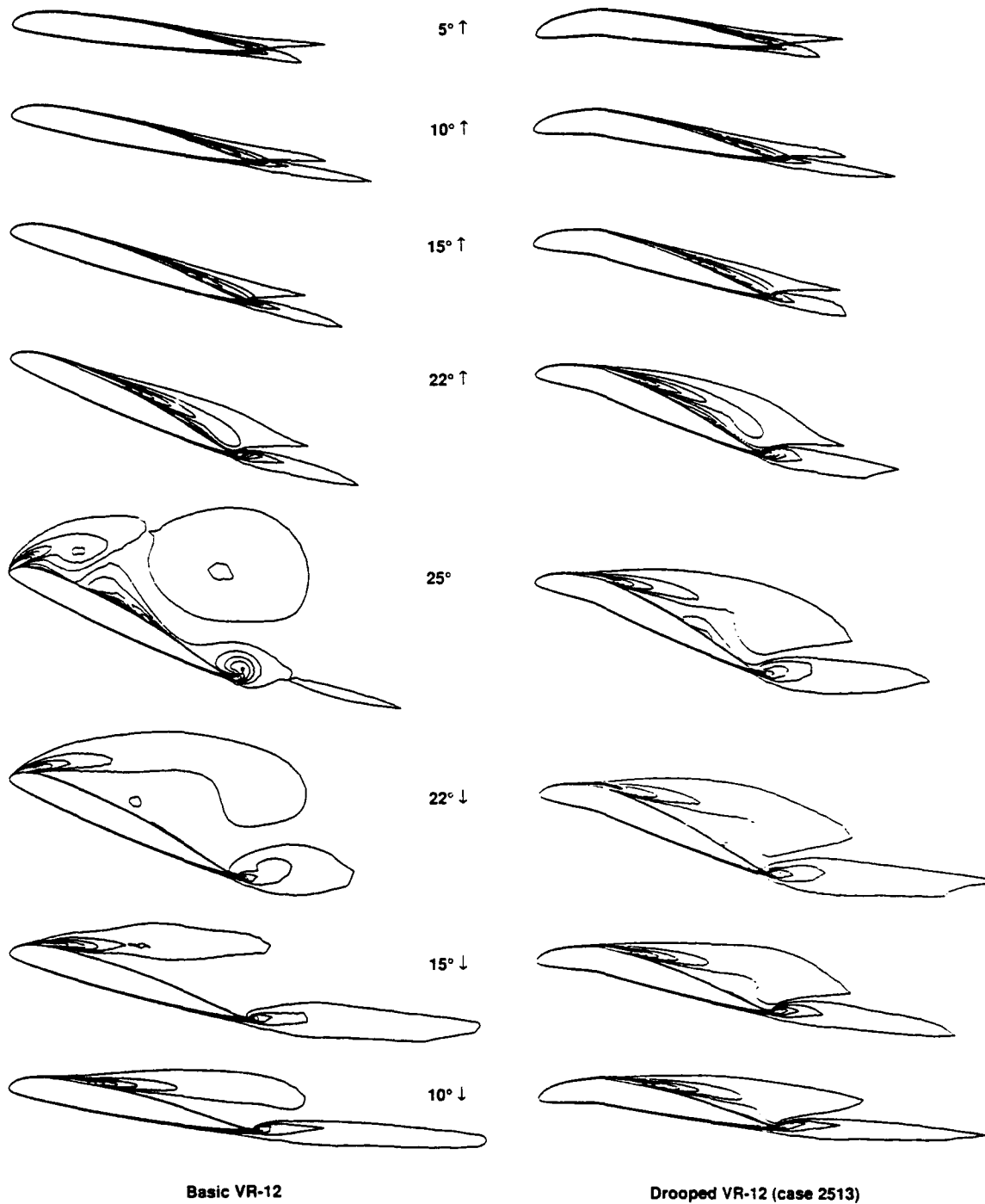
[Fig. 12] Evolution of the surface pressure distribution and streamlines of the basic VR-12 airfoil during oscillation at conditions of $Re = 2,000,000., \alpha = 15° + 10°sin\omega t, k = 0.1$.

16
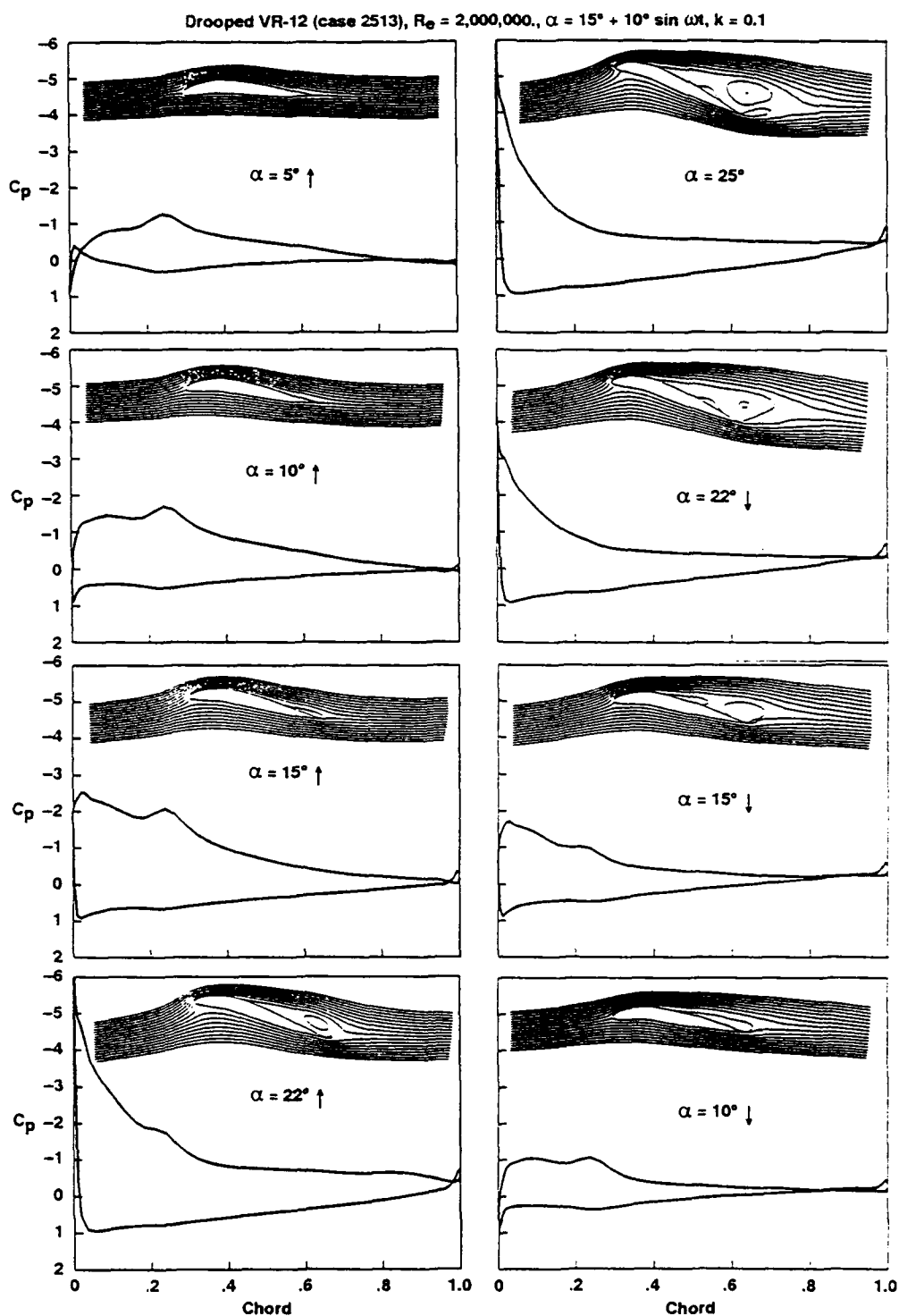
[Fig. 13] Evolution of the surface pressure distribution and streamlines of the drooped (case2513) VR-12 airfoil during oscillation at conditions of $Re = 2,000,000.$, $\alpha = 15° + 10° sin\omega t$, $k = 0.1$.

17

R_e = 2 million, α = 15° + 10° sin ωt, k = 0.1

| | 5° ↑ | |
| 10° ↑ |
| 15° ↑ |
| 22° ↑ |
| 25° |
| 22° ↓ |
| 15° ↓ |
| 10° ↓ |

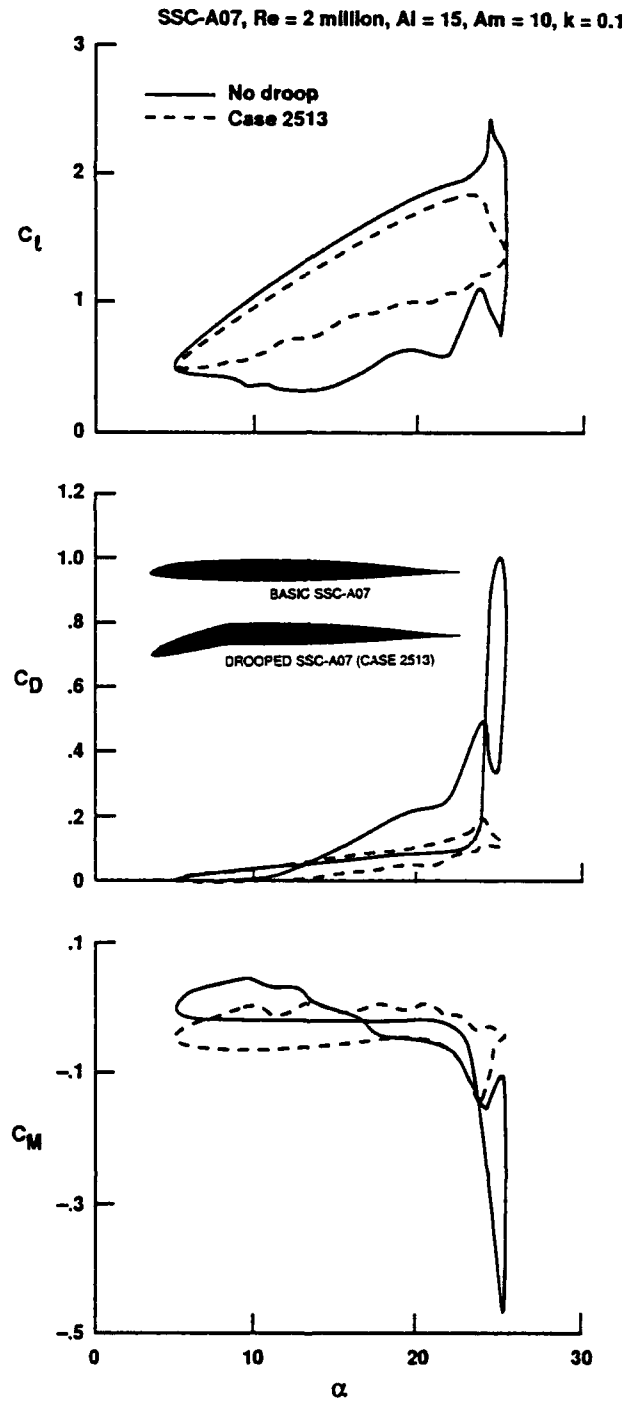Basic VR-12   Drooped VR-12 (case 2513)

[Fig. 14] Comparison of the vorticity contour developments of the basic and the drooped (case2513) VR-12 airfoil during oscillation at conditions of $Re = 2,000,000.$, $\alpha = 15° + 10° sin \omega t$, $k = 0.1$.

18
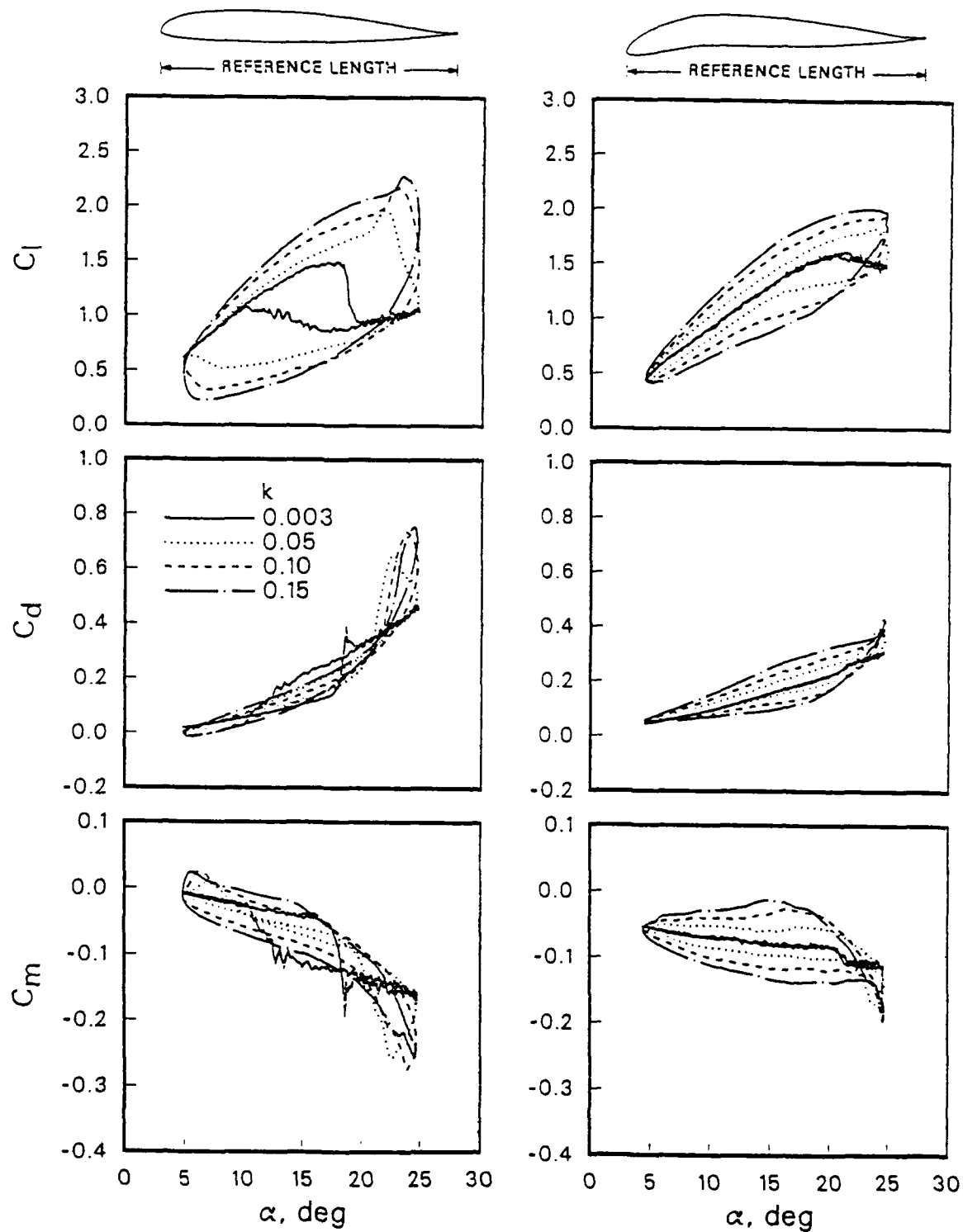
[Fig. 15] The effects of reduced frequency on the measured dynamic loads of both the basic and the drooped VR-12 airfoils at conditions of $Re = 200,000., \alpha = 15° + 10°sin\omega t, k = 0.1$.
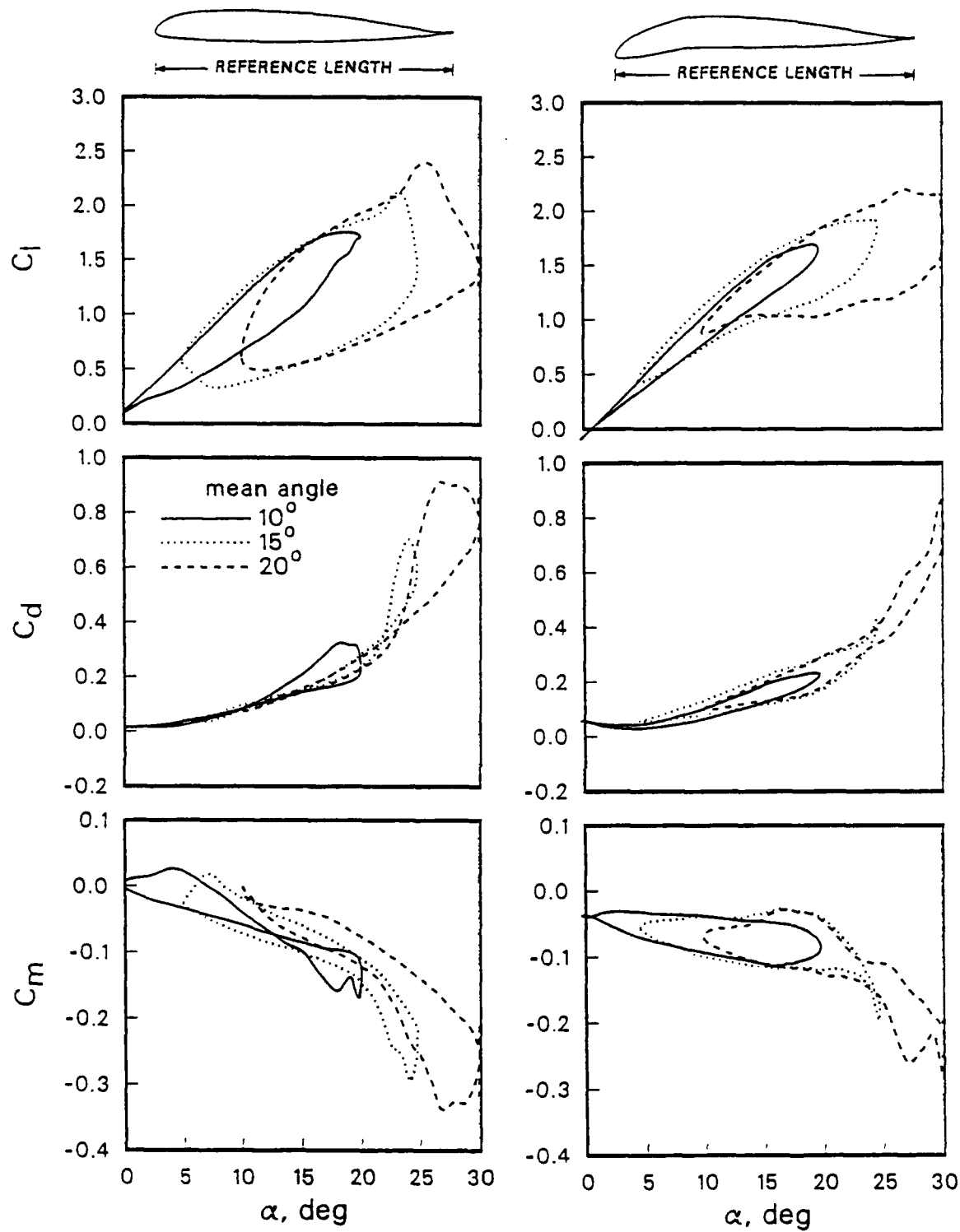
[Fig. 16] The effects of mean angle of oscillation on the measured dynamic loads of both the basic and the drooped VR-12 airfoils at conditions of $Re = 200,000., \alpha = 15° + 10° sin \omega t, k = 0.1$.

SSC-A07, Re = 2 million, Al = 15, Am = 10, k = 0.1

No droop
Case 2513

BASIC SSC-A07

DROOPED SSC-A07 (CASE 2513)

[Fig. 17] Calculated dynamic loads of both the basic and the drooped SSC-A07 airfoils at conditions of $Re = 2,000,000., \alpha = 15° + 10° sin\omega t, k = 0.1$.

21